Inertial Navigation and Visual Line Following for a Dynamical Hexapod Robot

Sarjoun Skaff, George Kantor, David Maiwand, Alfred A. Rizzi

{sarjoun, kantor, dm597, arizzi}@ri.cmu.edu

The Robotics Insititute, Carnegie Mellon University, Pittsburgh, PA

Abstract—This paper presents preliminary development of autonomous sensor-guided behaviors for a six-legged dynamical robot (RHex). These behaviors represent the first exteroceptive closed-loop locomotion strategies for this system. Simple motion models for RHex are described and used to deploy controllers for inertial straight line locomotion and visual line following. Results are experimentally validated on the robot.

I. INTRODUCTION

Sensor guided behaviors are essential for the autonomy of mobile robots. This paper reports the development of preliminary behavioral autonomy for a compliant hexapod robot (RHex - Robot Hexapod, http://www.rhex.net) using on-board inertia and vision sensors. RHex, shown in Figure 1, is a 47 x 40 x 24 cm, 8.5Kg, power-autonomous robot which locomotes by coordinating the motion of six independent legs rotating around the hips. Synchronizing the legs three by three, the robot produces alternating tripod gaits which behaviorally resemble that of a bipedal Spring Loaded Inverted Pendulum (SLIP) [1]. Varying the rate of leg re-circulation and structure of leg synchronization allows the robot to walk, jog, run and turn [2].

The robot's operation, however, is restricted to direct human control, constraining the operational range to the operator's line of sight. Furthermore, high speed motions such as running are difficult to control and require complete attention from the operator. These restrictions are mitigated through the application of autonomous behaviors and navigational aids.

Inertial guidance primarily enables straight-line motions. Guided by an on-board gyroscope, the behavior compensates for heading variations induced by the naturally swaying stride, and provides the operator with direct control of the robot's heading. Inertial rate information is measured at 300Hz, supporting high-rate control of heading. This control further enables motions such as turning at an operator-specified rate.

Visual guidance enables robot motion which is registered to environmental features. To demonstrate this capability, two types of line following behaviors are explored, corresponding to the two forms of visual servoing controllers found in the literature [3]. The first is a position-based controller which computes error in the robot workspace. The second is an image-based controller which computes error directly from image features. The latter strategy has the further benefit of respecting field
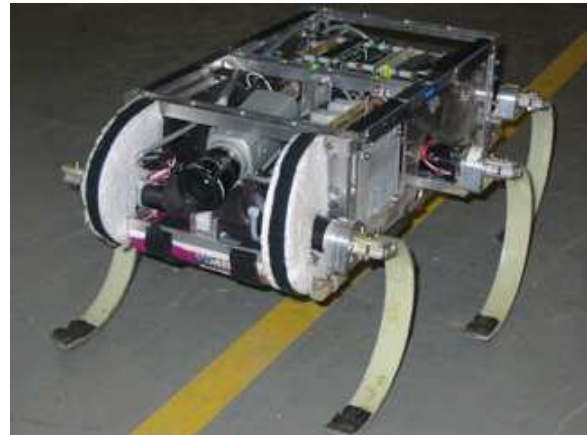

Fig. 1. RHex straddling a line.

of view constraints. Both of these guidance strategies free the operator from needing to continuously command to the robot.

The development of this small set of autonomous behaviors constitutes a first step toward operational autonomy for RHex. It further provides insight as to the validity of simple motion models for dynamically complex mobile platforms such as RHex.

A. Previous Work

The capability of following a line is useful for guiding autonomous platforms such as unmanned aerial vehicles. Whang [4] proposes to guide aircraft through waypoints connected by straight lines. The controller relies on first order motion models and maintains the aircraft within bounded heading accelerations. The controller's experimental validation, however, is limited to simulation.

Line following can also be viewed as a special case of trajectory tracking, a field addressed by a large body of literature. Some work focuses on sensor-based path planning and other on motion control or a combination of planning and execution.

Lee [5], for example, proposes a control policy for a robot tracking trajectories under saturation constraints. Diaz [6] presents an asymptotically stable nonlinear controller for unicycle trajectory tracking. Kwolek [7], on the other hand, addresses the sensor-based planning problem by proposing a stable control law for path following using on-board vision. Ma [8] derives piece-wise smooth

controllers for trajectory tracking directly in image space. The work presented here also centers on sensor-based navigation, but adopts simple control policies to evaluate their efficacy on robots with complex dynamics.

Similarly to the work of Murrieri [9], the approach taken here on FOV constrained navigation is inspired by Lyapunov theory, but offers the additional advantage of avoiding nonsmooth switching.

II. APPROACH

Three approaches for sensor-guided behavior are described here. The first is a controller that uses inertial sensing to steer the robot and the remaining two are vision–based line following controllers.

A. Motion Models for RHex (Templates)

The SLIP and Lateral Leg Spring (LLS) [10] templates describe RHex's motion in the sagital and horizontal planes, respectively. These models have limited application for robot control, however, because their anchoring in the physical system is yet unavailable.

A simpler horizontal motion model is the kinematic unicycle. Similarly to unicycles, RHex is subject to non-holonomic constraints preventing lateral motion and is controlled through forward and rotational velocities. System identification of the steering behavior indicates that accurate unicycle models grow in comlexity as the robot gains speed [11]. In the standard unicycle coordinates encoding position and orientation (Figure 2), the kinematics are written as

$$\frac{d}{dt} \begin{bmatrix} x \\ y \\ \theta \end{bmatrix} = \begin{bmatrix} v_f \cos\theta \\ v_f \sin\theta \\ 0 \end{bmatrix} + \begin{bmatrix} 0 \\ 0 \\ u \end{bmatrix}. \quad (1)$$

Here the control inputs are u and v_f, specifying the angular and forward velocities of the robot, respectively.
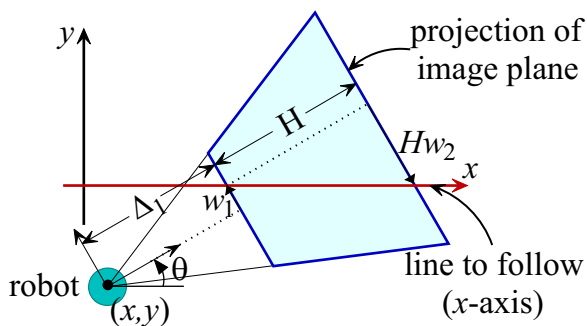

Fig. 2. Simplified model of robot and camera configurations, top view.

B. Inertia-guided Navigation

The purpose of inertial guidance is to control the robot's heading at all speeds. Experiments show that adjusting the gait offset directly controls the angular velocity [2], affecting only the third row of (1). To accomplish heading control, u is set proportional to the heading error,

$$u = \kappa_p \left(\theta - \bar\theta \right), \quad (2)$$

with θ and $\bar\theta$ representing the current and desired heading of the robot, respectively.

As predicted by [11], the complexity of the steering dynamics increases at running speed. Empirical evidence suggests that the heading dynamics are better modeled as a second order system of the form

$$\ddot\theta = -d\dot\theta + u, \quad (3)$$

with $d > 0$. Accordingly, at running speed, the policy

$$u = \kappa_p \left(\theta - \bar\theta \right) + \kappa_d \left(\dot\theta - \dot{\bar\theta} \right) \quad (4)$$

stabilizes the heading dynamics of (3).

C. Vision-guided Line Following

For the line following controller, RHex is modeled as a kinematic unicycle with a constant, known forward velocity v_f in (1).

1) Position-based controller: This controller minimizes the robot's relative distance, y, and angle, θ, to the line. An approximate motion model is derived from (1) by disregarding x and linearizing around $y = 0$ and $\theta = 0$, resulting in

$$\frac{d}{dt} \begin{bmatrix} y \\ \theta \end{bmatrix} = \begin{bmatrix} v_f \theta \\ 0 \end{bmatrix} + \begin{bmatrix} 0 \\ u \end{bmatrix}. \quad (5)$$

Equation 5 represents a second order system of the form $\ddot y = v_f u$, which can be stabilized by the control policy

$$u = \kappa_p y + \kappa_d \theta. \quad (6)$$

Experiments described in Section III demonstrate the validity of this approach at walking and jogging speeds. At running speed, however, second-order dynamics result in loss of regulation. Here, rather than directly commanding the gait offset, the same policy, (6), is used to command $\bar\theta$ of the inertial guidance controller (4). The result is a control policy that compensates for the second order effects and enables line tracking with reasonable efficacy.

2) FOV Respecting Controller: This controller uses camera-friendly coordinates to guarantee maintaining camera field of view (FOV) constraints while guiding the robot to the line.
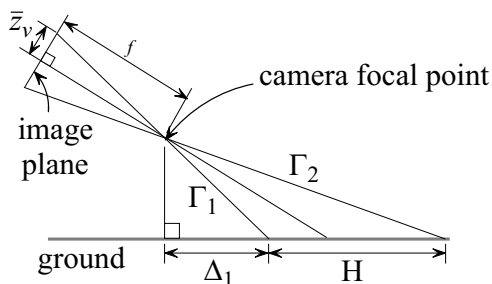

Fig. 3. Camera configuration, side view.

a) w-space Coordinates: For the purposes of vision-based line following, the control is performed in a carefully defined transformation of the sensor space. Let z_1 be the horizontal coordinate of the point at which the line, projected into the image plane, intersects the top of the image plane. Similarly, define z_2 to be the horizontal coordinate of the point at which the line intersects the bottom of the image plane. The w-space coordinates are then defined by

$$w_1 = \frac{\Gamma_1}{\eta} z_1$$
$$w_2 = \frac{1}{\eta H} (\Gamma_2 z_2 - \Gamma_1 z_1),$$

where $\eta = \sqrt{f^2 + \bar{z}_v^2}$. Here, f, $\bar{z}_v$, H, Γ_1, and Γ_2 are defined in Figures 2 and 3. In terms of the standard unicycle coordinates, w_1 and w_2 can be rewritten as

$$w_1 = \Delta_1 \tan\theta + \frac{y}{\cos\theta}$$
$$w_2 = \tan\theta ,$$

where Δ_1 is defined in Figure 3. Using this relationship, the unicycle kinematics (1) can be written in w-space as

$$\frac{d}{dt} \begin{bmatrix} w_1 \\ w_2 \end{bmatrix} = \begin{bmatrix} v_f w_2 \\ 0 \end{bmatrix} + \begin{bmatrix} \Delta_1 + w_1 w_2 \\ 1 + w_2^2 \end{bmatrix} u. \quad (7)$$

Clearly, regulating this system to $w = 0$ and holding it there is equivalent to following the line at velocity v_f. As a result, the line following problem is solved by finding a closed loop policy for u that stabilizes (7).

b) Field of View Constraints: In addition to achieving line following by stabilizing (7), the controller will ensure that the line intersects both the top and bottom of the image at all times. In w-space, this leads to following set of inequalities

$$|w_1| \leq \Gamma_1 \frac{\bar{z}_h}{\eta}$$
$$\frac{-\Gamma_2}{\eta} \bar{z}_h - w_1 \leq H w_2 \leq \frac{\Gamma_2}{\eta} \bar{z}_h - w_1, \quad (8)$$

where $\bar{z}_h$ is half the image width. Define Ω to be the set of all w such that the inequalities of (8) are satisfied. The set Ω is a parallelogram in the w_1-w_2 plane as shown in Figure 4.
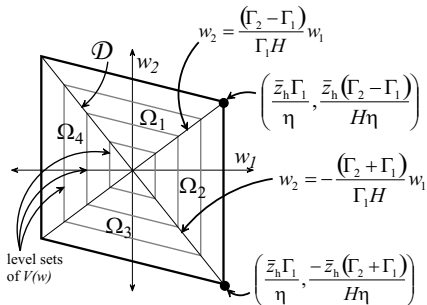

Fig. 4.   FOV boundaries represented in w-space.

This naturally leads to a precise formulation for the FOV-constrained line following problem as

Problem 1 (FOV constrained line following): Find a steering policy $u : \mathbb{R}^2 \to \mathbb{R}$ such that the closed loop system that results from applying u to (7) has the following properties:

1) $w = 0$ is an asymptotically stable equilibrium point.
2) The region of attraction for $w = 0$ includes all of Ω.
3) Ω is positive invariant.

Proposition 1: If the camera parameters satisfy the inequality

$$4H f^2 \left((\Gamma_1 + \Gamma_2)\Delta_1 + \Gamma_1 H \right) > \Gamma_1 (\Gamma_1 + \Gamma_2)^2 \bar{z}_h^2, \quad (9)$$

then the steering policy

$$u(w) = -k_1(w)w_2 - k_2 L w \quad (10)$$

with

$$k_1(w) = \frac{(\Gamma_1 + \Gamma_2)v_f}{(\Gamma_1 + \Gamma_2)(\Delta_1 + w_1 w_2) + \Gamma_1 H(1 + w_2^2)}$$

and

$$L = \begin{bmatrix} \dfrac{(\Gamma_1 + \Gamma_2)}{\Gamma_1 H} & 1 \end{bmatrix}$$

solves the FOV constrained line following problem (Problem 1) for any constant $k_2 \in \mathbb{R}$ that satisfies

$$\frac{v_f}{\Delta_1} > k_2 > v_f \frac{\Gamma_2 - \Gamma_1}{2\Gamma_2}.$$

Intuitively, the $-k_1(w)w_2$ term pushes the state parallel to the parallelogram diagonal $\mathcal{D}$ (see Figure 4) and toward the w_1-axis at every point in w-space. The $-k_2 L w$ term pushes the state toward $\mathcal{D}$. The result is a kind of parallel composition of behaviors that simultaneously pushes the state toward $\mathcal{D}$ and along $\mathcal{D}$ toward the origin.

More formally, consider a Lyapunov-like function V with level sets that are concentric parallelograms similar (in the geometric sense) to the one shown in Figure 4. Let $V : \mathbb{R}^2 \to \mathbb{R}$, $w \mapsto \gamma$, where the value of γ is proportional to the distance between the origin and the point at which the right edge of the parallelogram containing w intersects the w_1 axis. Proposition 1 is proved by showing that the policy (10) guarantees $\dot{V}(w) < 0$ for all $w \neq 0$. To facilitate the proof, Ω is divided into four open subregions as shown in Figure 4. V can then be written

$$V(w) = \begin{cases} \frac{1}{\Gamma_2} w_1 + \frac{H}{\Gamma_2} w_2 & \text{if} \quad w \in \Omega_1 \\ \frac{1}{\Gamma_1} w_1 & \text{if} \quad w \in \Omega_2 \\ -\frac{1}{\Gamma_2} w_1 - \frac{H}{\Gamma_2} w_2 & \text{if} \quad w \in \Omega_3 \\ -\frac{1}{\Gamma_1} w_1 & \text{if} \quad w \in \Omega_4 \end{cases} \quad (11)$$

On Ω_1: $\frac{\partial V}{\partial w} = \begin{bmatrix} \frac{1}{\Gamma_2} & \frac{H}{\Gamma_2} \end{bmatrix}$. Using the chain rule and substituting from (7) and (10) yields

$$\dot{V} = v_f w_2 + \left[\Delta_1 + w_1 w_2 + H(1 + w_2^2) \right]$$
$$(-k_1(w)w_2 - k_2 L w)$$
$$\triangleq v_f w_2 + A \left(-k_1(w)w_2 - k_2 L w \right)$$

Condition (9) guarantees that $A > 0$ for $w \in \Omega$, so the condition $\dot{V} > 0$ becomes

$$A k_2 L w > v_f w_2 - A k_1 w_2$$
$$= v_f w_2 - \frac{\left(\Delta_1 + w_1 w_2 + H(1 + w_2^2)\right)(\Gamma_1 + \Gamma_2)v_f w_2}{\left(\Delta_1 + w_1 w_2 + H(1 + w_2^2)\right)(\Gamma_1 + \Gamma_2) - \Gamma_2 H(1 + w_2^2)}.$$

Note that since $\Gamma_2 H(1 + w_2^2) > 0$, the absolute value of large fraction in the last line is greater than $|v_f w_2|$. This, together with the fact that $w_2 > 0$ on Ω_1 ensures that the right hand side is negative. Since $Lw > 0$ on Ω_1, $\dot{V} < 0$ for any $k_2 > 0$.

On Ω_2: $\frac{\partial V}{\partial w} = \begin{bmatrix} \frac{1}{\Gamma_1} & 0 \end{bmatrix}$. Using the chain rule and substituting from (7) and (10) yields

$$\dot{V} = v_f w_2 + (\Delta_1 + w_1 w_2)\left(-k_1(w)w_2 - k_2 Lw\right).$$

This argument proceeds by looking at four cases based on the signs of w_2 and $(\Delta_1 + w_1 w_2)$:

case 1: $w_2 > 0$
$w_2 > 0 \Rightarrow (\Delta_1 + w_1 w_2) > 0$, and the condition $\dot{V} < 0$ can be re-written

$$k_2 Lw > \frac{v_f w_2}{\Delta_1 + w_1 w_2} - k_1(w)w_2$$
$$= v_f w_2 \left(\frac{1}{\Delta_1 + w_1 w_2} - \frac{\Gamma_1 + \Gamma_2}{(\Gamma_1 + \Gamma_2)(\Delta_1 + w_1 w_2) + \Gamma_1 H(1 + w_2^2)}\right)$$
$$\triangleq v_f w_2 \beta.$$

Careful inspection and using the fact that $w_1 > 0$ on Ω_2 yields $0 < \beta < \frac{1}{\Delta_1}$, so this case can be proven by showing that

$$k_2 \left(\frac{\Gamma_1 + \Gamma_2}{\Gamma_1 H} w_1 + w_2\right) > \frac{v_f w_2}{\Delta_1}.$$

Dividing both sides by w_2 yields

$$k_2 \left(\frac{\Gamma_1 + \Gamma_2}{\Gamma_1 H} \frac{w_1}{w_2} + 1\right) > \frac{v_f}{\Delta_1}.$$

Since $\frac{w_1}{w_2} > 0$, the condition $k_2 > \frac{v_f}{\Delta_1}$ guarantees that $\dot{V} < 0$.

case 2: $w_2 < 0$, $(\Delta_1 + w_1 w_2) > 0$
Here, the condition $\dot{V} < 0$ can be re-written

$$\frac{v_f w_2}{\Delta_1 + w_1 w_2} - k_1(w)w_2 < k_2 Lw,$$

which is equivalent to

$$\frac{v_f}{\Delta_1 + w_1 w_2} - k_1(w) > k_2 \left(\frac{\Gamma_1 + \Gamma_2}{\Gamma_1 H} \frac{w_1}{w_2} + 1\right). \qquad (12)$$

The fact that $w_1 w_2 < 0$ and that $\frac{w_1}{w_2} < \frac{\Gamma_1 H}{\Gamma_2 - \Gamma_1}$ on Ω_2 shows that (12) is implied by

$$\frac{v_f}{\Delta_1} - \frac{(\Gamma_1 + \Gamma_2)v_f}{(\Gamma_1 + \Gamma_2)\Delta_1 + \Gamma_1 H} > k_2 \left(\frac{\Gamma_1 + \Gamma_2}{\Gamma_2 - \Gamma_1} + 1\right).$$

By inspection, the left hand side of this inequality is less than v_f, so $\dot{V} < 0$ provided that

$$k_2 < v_f \frac{\Gamma_2 - \Gamma_1}{2\Gamma_2}.$$

case 3: $w_2 < 0$, $(\Delta_1 + w_1 w_2) = 0$
The condition $\dot{V} < 0$ becomes $v_f w_2 < 0$, which is clearly true for this case.

case 4: $w_2 < 0$, $(\Delta_1 + w_1 w_2) < 0$
Here, $\dot{V} < 0$ is equivalent to

$$\frac{v_f w_2}{\Delta_1 + w_1 w_2} - k_1(w) < k_2 Lw.$$

Both terms on the left hand side are negative, and the term Lw is positive on Ω_2. As a result, this case is solved for any $k_2 > 0$.

Note that due to the symmetry inherent in boundaries and steering policy, similar arguments can be used to show that $\dot{V} < 0$ on Ω_3 and Ω_4. As a result, $\dot{V} < 0$ everywhere

in Ω under the conditions of the Proposition, which yields asymptotic stability of the origin. Positive invariance in Ω is guaranteed by the fact that the boundaries of Ω coincide with a level set of V.

III. RESULTS

A. Inertia-guided Navigation

The performance of the inertia-guided controller is evaluated through two metrics. Since the task is to maintain RHex's heading, the first metric is the average deviation of the robot from the reference heading under steady state operation. The second metric measures the reactivity of the controller and is expressed by its settling time following a step change in reference heading.

1) Straight Line Navigation: Straight line locomotion is achieved through application of the controllers of Section II-B. Gains for the controllers are experimentally tuned to provide near critically-damped steering. Figure 5 shows a typical run at jogging speed, where the robot's heading is successfully controlled. The figure also demonstrates that the heading oscillates at approximately 2Hz, the characteristic jogging stride frequency.

To evaluate the controller's performance, the reference heading is abruptly changed and the robot's reaction is observed as the controller converges to the new reference. A battery of experiments indicate that the robot resumes steady state operation within approximately 2 seconds of a 15-degree disturbance (Figure 6).
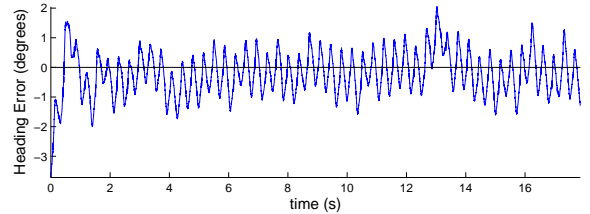
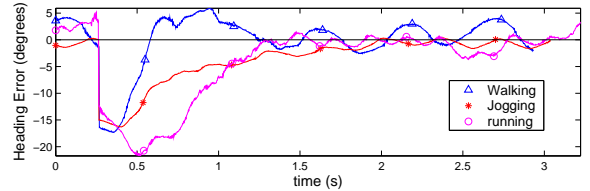Fig. 5. RHex's heading at jogging speed under inertial guidance.

Fig. 6. RHex's heading as it reacts to a 15 degree disturbance at walking, jogging and running speeds under inertial guidance.

Table I summarizes the performances achieved at the three speeds over flat terrain. It is worth noting that the average angular deviation achieved at jogging speed is notably smaller than that at walking speed - the implication is that the robot's motion approximates that of a unicycle more accurately when jogging. At running speed, substantial motion dynamics induce greater deviations.

2) Impact of inertia-guided navigation on robot operations: The advantage of relying on the gyroscope for guidance is emphasized when the robot operates in challenging environments. Over rough terrain, for example,

Speed	Walking	Jogging	Running
Runs	5	5	5
Average	1.26	0.64	5.10
Maximum	3.78	5.30	34.27
Standard deviation	0.75	0.52	5.09

TABLE I

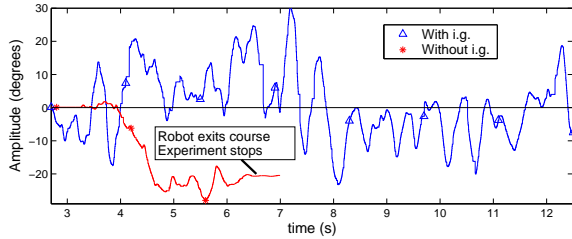HEADING DEVIATION (IN DEGREES) UNDER STEADY-STATE INERTIAL GUIDANCE

Fig. 7.   RHex's heading while walking on a 15-cm rock bed, with and without inertial guidance.

RHex has difficulty maintaining its heading. The inertia-guided controller helps overcome this problem and enables navigation through pebbles and rocks in a relatively straight line. Figure 7 showcases the contrast between the two situations. The task here consists in traversing a 10m-long testbed filled with uneven rocks. Left to itself, RHex is soon thrown off course. With inertial guidance, the robot successfully completes the course despite large heading oscillations due to the ruggedness of the terrain.

Table II reports the performance of the straight-line controller on different surfaces. As expected, the average angular misalignment grows with the ruggedness of the terrain. The controller successfully maintains the robot on a relatively straight line in all experiments.

The inertia-guided controller also steers the robot at user-specified turning rates. By varying the reference heading over time, it is possible to drive RHex through controlled trajectories. Figure 8 depicts the orientation of RHex as it tracks a monotonically increasing reference heading, effectively driving the robot on an arc of constant radius.

B. Vision-guided Navigation

As with inertial guidance, two measures are used to quantify the controller's performance. With the goal of

| Terrain | Sand | Carpet | Pebbles | Rocks |
	fine grain	with 12cm pipes	5cm dia.	15cm dia.
Runs	6	5	5	3
Average	2.21	3.82	3.12	8.97
Maximum	7.64	20.59	12.57	35.25
Std. dev.	1.74	3.36	3.38	7.48

TABLE II

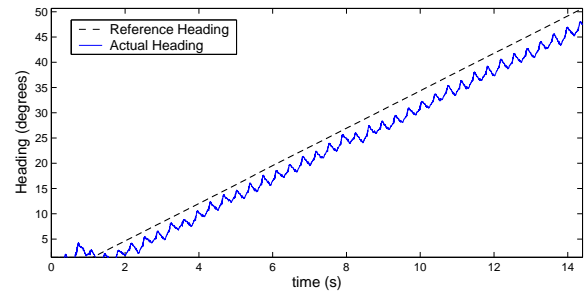TERRAIN-SPECIFIC HEADING DEVIATION AT WALKING SPEED UNDER INERTIAL GUIDANCE.

Fig. 8.   RHex's reference and actual heading while turning at 5 degrees/s at jogging speed.

following the line at all time, a natural metric is the average distance between the robot and the line. The second metric assesses the system's reactivity by measuring its settling time as it responds to a step input.

The experimental setup is shown in Figure 1. RHex uses a Sony DFW-V300 camera operating at 30Hz to detect a 3cm-wide yellow tape laid on the ground. Vision software extracts the line through color segmentation at camera frame-rate, utilizing a PC104+, 300Mhz Pentium-II class embedded computer.

Figure 9 is a representative plot of the robot's distance to the line being followed. The average distance is less than a centimeter at walking speed, a small error relative to the size of the robot and the distance traveled (30m). Another measure of the controller's performance is its reaction to step input, expressed here in terms of settling time. The experimental procedure consists in positioning the robot off the line and observing its behavior as the controller converges. When experiencing a 30 cm disturbance, the settling time of the linear controller is about 4s at walking and jogging speeds (Figure 10). The nonlinear controller's settling time is about 2.5 seconds at walking speed and 5 seconds at jogging speed. The step response at running speed is not measured because substantial dynamics prevent the engineering of consistent disturbances.
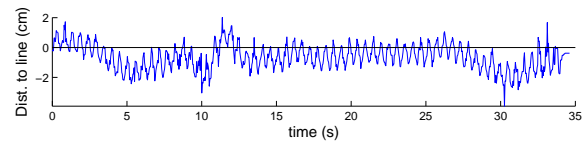

Fig. 9.   RHex's distance to line versus time, at walking speed, under linear, vision-based control.
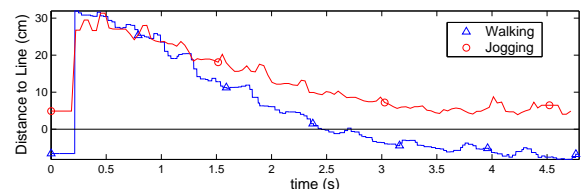

Fig. 10.   RHex's distance to line as it recovers from a 30cm lateral disturbance, under linear, vision-based control.

Speed	Walking		Jogging		Running
	linear	*nonlinear*	*linear*	*nonlinear*	*linear*
Runs	5	5	5	5	5
Average	0.94	0.75	6.38	2.32	8.82
Maximum	17.68	6.48	13.11	7.07	31.08
Std. dev.	1.32	0.62	1.96	1.43	6.32

TABLE III

DISTANCE TO LINE (IN CM) UNDER LINEAR AND NONLINEAR
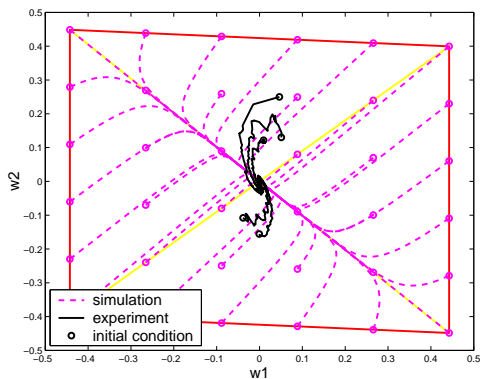VISION-BASED CONTROL.

Fig. 11. Simulated and experimental w-space trajectories for the nonlinear FOV respecting controller.

The performance results of the linear and nonlinear controllers are summarized in Table III. The maximum deviation for the linear controller at walking speed is surprisingly high, but it is due to a single outlier disturbance from which the controller promptly recovered. The average distance to line when running is reasonable relative to the slower speeds, but the large standard deviation reflects the swaying motions induced by the dynamics. The success is virtually 100% when walking and jogging, but only about 30% at running speed.

Figure 11 plots both simulated and experimental trajectories in the w_1-w_2 plane of the robot under the FOV respecting controller. The dashed lines represent simulated trajectories, and the plot shows that the state stays within the parallelogram (FOV boundaries) for initial conditions within the parallelogram. The solid lines plot some experimental trajectories, demonstrating that the behavior of the robot somewhat matches the simulation predictions. The controller is not tested for initial conditions near the FOV boundaries due to complexities of line detection in these areas.

IV. CONCLUSION

This paper presented the first successful deployment of sensor-guided behaviors on RHex. Controllers based on simple motion models enable inertial straight-line locomotion and visual line following. Experiments validate the operational performance of the behaviors and provide insight as to their limitation. These results constitute a first step leading to sensor-guided operational autonomy for dynamic legged robots.

Ongoing research is extending sensor-based capabilities to include robot state-estimation through visual registration and inertial sensing. These efforts will enable robot localization, online tuning of gait parameters and improved locomotion notably at running speed and in unknown environments.

V. REFERENCES

[1] Uluc Saranli. *Dynamic Locomotion with a Hexapod Robot*. PhD thesis, University of Michigan, September 2002.

[2] U. Saranli, M. Buehler, and D. E. Koditschek. RHex: A Simple and Highly Mobile Robot. *International Journal of Robotics Research*, 20(7):616–631, July 2001.

[3] S. Hutchinston, G. D. Hager, and P. I. Corke. A tutorial on visual servo control. *IEEE Transactions on Robotics and Automation*, 12(5), October 1996.

[4] I. H. Whang and T. W. Hwang. Horizontal waypoint guidance design using optimal control. *IEEE Transactions on Aerospace and Electronic Systems*, 38(3):1116–1120, July 2002.

[5] T. Lee, K. Song, C. Lee, and C. Teng. Tracking control of unicycle-modeled mobile robots using a saturation feedback controller. *IEEE Transactions on Control Systems Technology*, 9:305–318, March 2001.

[6] F. Diaz del Rio., G. Jimenez, J. L. Sevillano, S. Vicente, and A. Civit Balcells. A generalization of path following for mobile robots. In *1999 IEEE International Conference on Robotics and Automation*, pages 7–12, Detroit, MI, May 1999.

[7] B. Kwolek, T. Kapuściński, and M. Wysocki. Vision-based implementation of feedback control of unicycle robots. In *Proceedings of the First Workshop on Robot Motion and Control*, pages 101–106, Piscataway, NJ, 1999. IEEE.

[8] Y. Ma, J. Kovseská, and S. Sastry. Vision guided navigation for a nonholonomic mobile robot. In D. Kriegman, G. Hager, and A. S. Morse, editors, *Lecture Notes in Control and Information Sciences 237*, pages 134–145. Springer, 1998.

[9] P. Murrieri, D. Fontanelli, and A. Bicchi. Visual-servoed parking with limited view angle. In B. Siciliano and P. Dario, editors, *Experimental Robotics VIII, STAR 5*, pages 265–274. Springer-Verlag, Berlin Heidelberg, 2003.

[10] J. Schmitt and P. Holmes. Mechanical models for insect locomotion: Dynamics and stability in the horizontal plane - I. Theory. *Biological Cybernetics*, 83:501–515, April 2000.

[11] D. Maiwand. System identification, using vision-based localisation, for a hexapod robot. Master's thesis, Carnegie Mellon University, May 2003.